2021 43rd Annual International Conference of the
IEEE Engineering in Medicine & Biology Society (EMBC)
Oct 31 - Nov 4, 2021. Virtual Conference

Improving Minimum Variance Beamforming with Sub-Aperture Processing for Photoacoustic Imaging

Rashid Al Mukaddim, Rifat Ahmed and Tomy Varghese

***Abstract*— Minimum variance (MV) beamforming improves resolution and reduces sidelobes when compared to delay-and-sum (DAS) beamforming for photoacoustic imaging (PAI). However, some level of sidelobe signal and incoherent clutter persist degrading MV PAI quality. Here, an adaptive beamforming algorithm ($PSAP_{MV}$) combining MV formulation and sub-aperture processing is proposed. In $PSAP_{MV}$, the received channel data are split into two complementary nonoverlapping sub-apertures and beamformed using MV. A weighting matrix based on similarity between sub-aperture beamformed images was derived and multiplied with the full aperture MV image resulting in suppression of sidelobe and incoherent clutter in the PA image. Numerical simulation experiments with point targets, diffuse inclusions and microvasculature networks are used to validate $PSAP_{MV}$. Quantitative evaluation was done in terms of main-lobe-to-side-lobe ratio, full width at half maximum (FWHM), contrast ratio (CR) and generalized contrast-to-noise ratio (gCNR). $PSAP_{MV}$ demonstrated improved beamforming performance both qualitatively and quantitatively. $PSAP_{MV}$ had higher resolution (FWHM =0.19 mm) than MV (0.21 mm) and DAS (0.22mm) in point target simulations, better target detectability (gCNR =0.99) than MV (0.89) and DAS (0.84) for diffuse inclusions and improved contrast (CR in microvasculature simulation, DAS = 15.38, MV = 22.42, $PSAP_{MV}$ = 51.74 dB).**

I. Introduction

Beamforming is a critical building block to ensure high quality photoacoustic imaging (PAI) with linear array clinical and pre-clinical imaging systems. Delay-and-sum (DAS) beamforming is commonly employed and preferred for its low computational complexity and real time capability. However, when DAS beamforming is applied to PAI, the resultant images suffer from resolution degradation and clutter corruption due to off-axis and sidelobe signal contributions [1]. Therefore, alternative beamforming algorithm development has been pursued in the PAI community. Several advanced PAI beamforming algorithms have been reported in literature for example minimum variance (MV) [1], coherence processing [2-6], delay-multiply-and-sum (DMAS) [7-9] and machine learning based image reconstructions [10-13]. In this paper, we focus on improving the performance of MV for PAI.

MV beamforming calculates optimal aperture weighting using data statistics in aperture domain to reduce contributions from off-axis signals. Park *et al.* adapted MV beamforming for PAI and demonstrated resolution improvement over DAS [1]. Mozaffarzadeh *et al.* combined both MV and eigen-based MV with DMAS to improve the resolution of DMAS beamforming [14, 15]. We have previously demonstrated the use of MV for *in vivo* cardiac PAI [4] and showed that incoherent clutter noise was not suppressed using only MV beamforming. Paridar *et al.* incorporated a sparse regularization constraint to the MV optimization problem improving performance [16]. Even though MV improves resolution and reduces sidelobes when compared to DAS, some level of sidelobe signals persist. One simple solution is to weight MV images with coherence factor [1, 4, 17, 18]. However, this may not be an ideal solution in low signal-to-noise ratio environments resulting in undesirable PA signal suppression [19]. In this paper, we propose to utilize a recently developed photoacoustic sub-aperture processing (PSAP) method [19] with MV to address the sidelobe corruption problem while preserving resolution improvement obtained with MV.

This work is funded in part by UW-Madison Office of the Vice Chancellor for Research and Graduate Education from the Wisconsin Alumni Research Foundation and National Institutes of Health Grants S10 OD018505 and 1R01 HL147866-01

R. A. Mukaddim and T. Varghese are with the Department of Medical Physics, University of Wisconsin (UW) School of Medicine and Public Health (SMPH), Madison. R Ahmed is with Department of Biomedical Engineering, Duke University. (e-mail: mukaddim@wisc.edu).

II. Theoretical Background

A. Delay-and-sum (DAS) Beamforming

Consider, a linear array ultrasound transducer with a *M*-element aperture that receives PA generated acoustic waves. These are stored in a column vector $\mathbf{X}(t)$ after applying element-wise delays, d_m for dynamic receive focusing. DAS beamforming defined as weighted sum of vector elements of $\mathbf{X}(t)$ represented as below:

$$\mathbf{DAS}(t) = \mathbf{W}(t)^H \mathbf{X}(t) \tag{1}$$

where, $\mathbf{W}(t)$ is the aperture weighting vector and t denotes time-of-arrival which is mapped into imaging depth assuming constant speed of sound in the propagating medium.

B. Minimum Variance (MV) Beamforming

MV beamforming [1, 4, 20] calculates $\mathbf{W}(t)$ by minimizing the variance of beamformed signals by solving the following optimization problem:

$$\min_{\mathbf{W}(t)} \mathbf{W}(t)^H \mathbf{R}(t)\mathbf{W}(t) \;\; \text{s.t.}\; \mathbf{W}(t)^H a = 1 \tag{2}$$

where, $\mathbf{R}(t)$ is the co-variance matrix and a is the steering vector. The solution using a Lagrange multiplier method results in a MV weighting vector:

$$\mathbf{W}_{\mathbf{MV}}(t) = \frac{\mathbf{R}(t)^{-1} a}{a^H \mathbf{R}(t)^{-1} a} \tag{3}$$

In practice, $\mathbf{R}(t)$ is replaced with $\mathbf{R}_{\mathbf{SA}}(t)$ by dividing the full array into overlapping sub-arrays with the sub-array length denoted by *S*. Finally, MV beamformed image can be represented as follows:

$$\mathbf{MV}(t) = \frac{1}{M-S+1}\sum_{s=1}^{M-S+1} \mathbf{W}_{\mathbf{MV}}(t)^H \mathbf{X}_s(t) \quad (4)$$

where, $\mathbf{X}_s(t)$ is the sub-array signal vector.

C. Photoacoustic Sub-aperture Processing (PSAP) for Minimum Variance (MV) Beamforming

We first generate two MV beamformed images, $MV_1(t)$ and $MV_2(t)$ using two non-overlapping sub-apertures having no common elements [19, 21, 22]. Then, 2-D normalized cross-correlation (NCC) between $MV_1(t)$ and $MV_2(t)$ is performed to separate on-axis main-lobe signals and interfering side-lobe signals. $NCC(t)$ is used to estimate a dynamic weighting matrix, $PSAP_W(t)$ using following equation:

$$\mathbf{PSAP}_{\mathbf{W}}(t) = \max(\mathbf{NCC}(t), \varepsilon) \quad (5)$$

where, ε is a minimum NCC threshold value to estimate a weighting matrix having a range of $[\varepsilon, 1]$ (ε=0.001, empirically chosen to distinguish between main and side lobe signals). Finally, $PSAP_W(t)$ is multiplied with $MV(t)$ resulting in a PSAP MV beamformed image denoted as $PSAP_{MV}(t)$. Here, we design the first sub-aperture with ones and zeros with an alternating pattern of N elements on and N elements off, with the second sub-aperture is complementary to the first one. For comparative studies, PSAP images were also derived using DAS images termed as $PSAP_{DAS}(t)$.

III. Materials and Methods

A. Numerical Simulation Study

The proposed method was validated using numerical simulations with point targets, diffuse inclusion and microvasculature networks. A point target phantom was designed with four 100 μm point targets placed equidistantly starting from a depth of 8 mm with an initial pressure magnitude of 3 Pa. PA channel data were simulated using the k-Wave toolbox [23]. Diffuse inclusion phantom contained two 3 mm-diameter circular targets with random spatial distribution of optical absorbers (299 absorbers/mm^2) [24]. For the microvasculature phantom, vascular images collected from the fundus oculi drive [25] were used [19]. For both inclusion and microvasculature simulations, a hybrid simulation framework [4] with MCMatlab [26] and k-Wave [23] toolbox was used. MCMatlab estimated the initial pressure distribution by performing optical simulation while PA channel data were derived using k-Wave. Optical simulation was done to model 95% oxygenated blood using an 850 nm laser irradiation wavelength with target and background absorption coefficients of 5.6 and 0.01 cm^{-1}, respectively. An acoustic receiver with 128-elements (72-μm element width, 18-μm kerf) operating at f_c = 21 MHz, 100% fractional bandwidth and 84 MHz sampling frequency was modelled.

B. Algorithm Implementation

DAS beamforming was performed with a 64-element aperture, uniform apodization and f-number of 1. MV beamforming used sub-arrays with length $S = 24$ and diagonal loading $\Delta = 1/(100 \times S)$ to estimate $\mathbf{R}_{SA}(t)$. PSAP parameters used are listed in Table I. Parameters were chosen based on previous studies reported in [19]. Algorithms were run using a GPU and MATLAB Parallel Computing toolbox for accelerated computation.

TABLE I: PSAP Parameters

Experiment	Parameter	Value
Point Target	Alternating elements (N)	16-16
	NCC Kernel (Wavelength, A-lines)	(4.5λ,3)
Diffuse Inclusion Microvasculature	Alternating elements (N)	2-2
	NCC Kernel (Wavelength, A-lines)	(1.5λ,3)

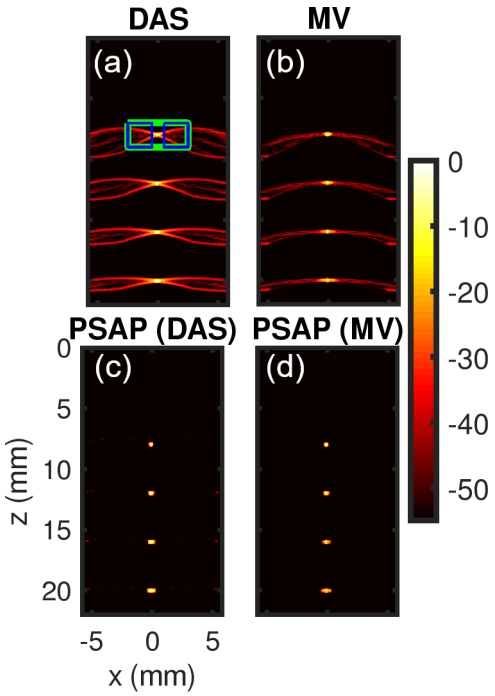

Fig. 1. Beamformed images from point target simulation. (a) DAS, (b) MV, (c) $PSAP_{DAS}$ and (d) $PSAP_{MV}$.

C. Quantitative Performance Analysis

For point target simulations, we computed the main-lobe-to-sidelobe (MLSL) ratio (dB) and full-width-at-half-maximum (FWHM) at -6 dB as follows [19]:

$$MLSL = 20 \times \log_{10}\left(\left(m_{\max} - m_{\min}\right)/\sigma_n\right) \quad (6)$$

where, $m_{\max}$ and $m_{\min}$ denote the maximum and minimum signal amplitude within a target rectangular region-of-interest (ROI) centered on each point (green ROI in Fig. 1 (a)) and σ_n represents the standard deviation from two noise ROIs (blue ROIs in Fig. 1 (a)) around the target ROI.

Diffuse inclusion and microvasculature simulations were quantified using contrast ratio (CR) and generalized contrast-to-ratio (gCNR) [27, 28]:

$$CR = 20 \times \log_{10}\left(m_t/m_b\right) \quad (7)$$

$$gCNR = 1 - \sum_{j=0}^{N_{bin}-1} \min\left\{k_t(x_j), k_b(x_j)\right\} \quad (8)$$

where, m_t and m_b denote average envelope PA signal amplitudes for target and background ROIs, respectively. For gCNR, k_t and k_b denote histograms with 1000 bins (N_{bin} with bin centers indicated by j and chosen empirically) derived from the target and background ROIs (mean ROI size = 838 pixels), respectively.

IV. Results and Discussion

Figures 1 (a) – (d) show point target beamformed images with DAS, MV, $PSAP_{DAS}$ and $PSAP_{MV}$ respectively. Note the presence of strong sidelobe signals with DAS. MV reduced sidelobes seen with DAS but does not suppress it completely. Incorporation of PSAP with both MV and DAS provided beamformed images with significant performance improvements over DAS and MV.

Figures 2 (a) – (b) show the point spread function (PSF) at a depth of 8 mm and 20 mm, respectively. $PSAP_{MV}$ and $PSAP_{DAS}$ have narrower PSFs with lowest sidelobe level. Tables II and III summarize the results for MLSL and FWHM comparison. Improvement in lateral resolution (lowest FWHM) and sidelobe reduction (highest MLSL) was achieved using $PSAP_{MV}$.

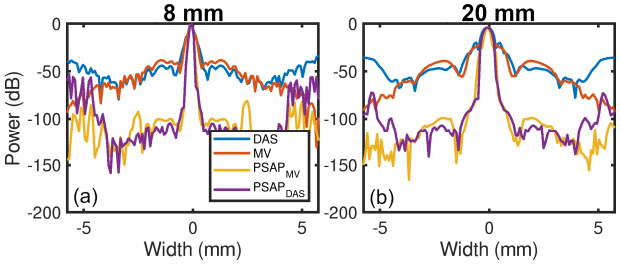

Fig. 2. Lateral PSF at depths of (a) 8 and (b) 20 mm, respectively.

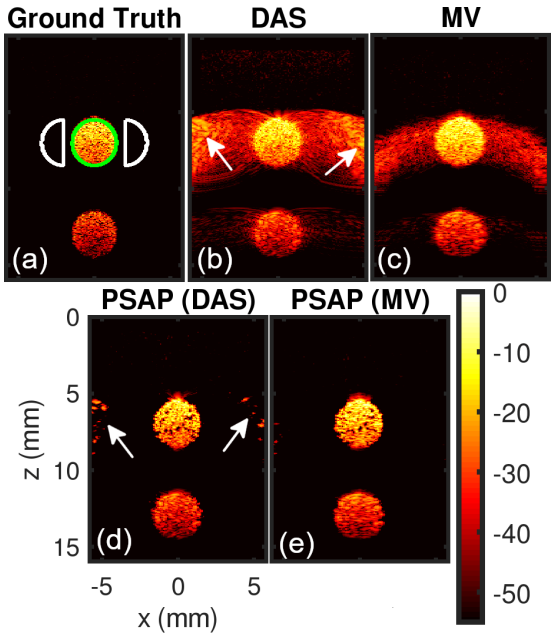

Fig. 3. Diffuse inclusion beamforming results. (a) Ground truth initial pressure distribution, (b) DAS, (c) MV (d) $PSAP_{DAS}$ and (e) $PSAP_{MV}$. Display dynamic range 55 dB.

Beamformed images for the diffuse inclusion simulation using DAS, MV, $PSAP_{DAS}$ and $PSAP_{MV}$ are shown in Figs. 3 (b) – (e). The ground truth initial pressure distribution with target (green circle) and background (white half-circles) ROIs is presented in Fig. 3 (a). For DAS, we observe high sidelobe signal levels specially near the borders for shallow targets as indicated by arrows (Fig. 3 (b)). MV results show significant image quality improvements with suppression of the strong border region clutter signals (Fig. 3 (c)). $PSAP_{DAS}$ further reduced sidelobes except for some noise signals near the borders (white arrows in Fig. 3 (d)). Highest performance enhancement with increased sidelobe suppression was achieved with $PSAP_{MV}$ (Fig. 3 (e)).

Table II: MLSL (dB) Results

	DAS	MV	$PSAP_{MV}$	$PSAP_{DAS}$
8 mm	41.15	50.84	**84.63**	67.98
12 mm	38.16	47.40	**107.85**	65.97
16 mm	35.91	46.89	**100.12**	65.62
20 mm	33.82	42.26	**95.05**	66.92

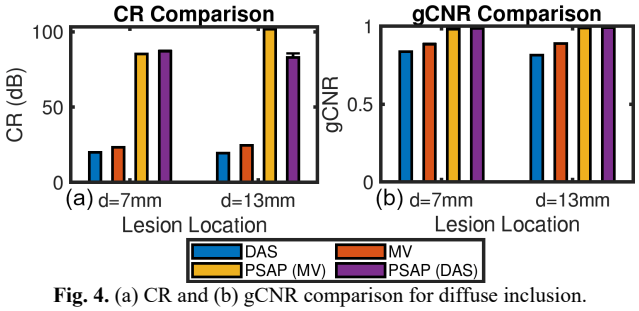

Fig. 4. (a) CR and (b) gCNR comparison for diffuse inclusion.

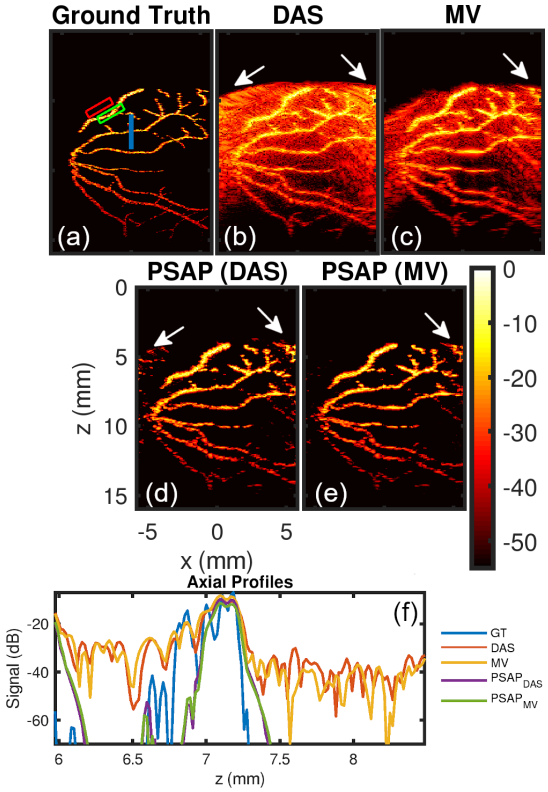

Fig. 5. Simulated microvasculature beamformed images. (a) Ground truth initial pressure distribution, b) DAS, (c) MV (d) $PSAP_{DAS}$ and (e) $PSAP_{MV}$, (f) axial profile comparison at a blue line ROI shown in fig. 5 (a). Display dynamic range 55 dB.

CR and gCNR comparison results for diffuse inclusion simulation are shown in Figs. 4 (a) – (b) respectively. $PSAP_{MV}$ and $PSAP_{DAS}$ demonstrated similar results with better CR and gCNR compared to DAS and MV alone. For example, mean gCNR values (n = 10) for the inclusion at 8 mm, for DAS = 0.84, MV = 0.89, $PSAP_{MV}$ = **0.98** and $PSAP_{DAS}$ = **0.99** demonstrate that improvement in both contrast and target detectability is achieved using PSAP for MV and DAS.

Figures 5 (b) – (e) show microvasculature beamformed images with DAS, MV, $PSAP_{DAS}$ and $PSAP_{MV}$, respectively.

The ground truth initial pressure distribution is presented in Fig. 5 (a). Note that DAS image suffer from high level of sidelobe signals specially near the borders for shallower vessels (white arrows in 5 (b)). Results using MV show suppression of the strong sidelobe signals but unexpected background clutter persist. $PSAP_{DAS}$ further reduced sidelobes except for some noise signals near the borders (white arrows in Fig. 5 (d)). Best quality image was achieved with $PSAP_{MV}$ (Fig. 5 (e)) showing a close resemblance with the ground truth image. CR and gCNR were computed by placing small rectangular ROIs covering the shallowest vessels as target ROIs (green ROI in Fig. 5 (a)) and then translating them into the sidelobe regions as background ROIs (red ROI in Fig. 5 (a)). $PSAP_{MV}$ had the highest CR and gCNR values (Mean CR [dB] for DAS = 15.38, MV = 22.42, $PSAP_{MV}$ = **51.74,** $PSAP_{DAS}$ = 43.64 and mean gCNR for DAS = 0.71, MV = 0.81, $PSAP_{MV}$ = **0.84,** $PSAP_{DAS}$ = 0.82).

TABLE III: FWHM (MM) RESULTS

	DAS	**MV**	**$PSAP_{MV}$**	**$PSAP_{DAS}$**
8 mm	0.22	0.21	**0.19**	0.19
12 mm	0.32	0.17	**0.16**	0.27
16 mm	0.41	0.22	**0.21**	0.34
20 mm	0.53	0.26	**0.25**	0.42

V. CONCLUSION

In this paper, a sub-aperture processing technique to suppress sidelobes and background clutter with MV beamforming have been reported and validated using numerical simulations. This hybrid beamforming algorithm coupled better resolution from MV with sidelobe signal suppression from PSAP. The resulting $PSAP_{MV}$ demonstrated higher contrast and improved target detectability. Future work will involve validation in more complicated simulation environments (e.g., addition of channel noise, acoustic attenuation), phantom experiments and *in vivo* applications.

REFERENCES

[1] S. Park, A. B. Karpiouk, S. R. Aglyamov, and S. Y. Emelianov, "Adaptive beamforming for photoacoustic imaging," *Optics letters,* vol. 33, pp. 1291-1293, 2008.

[2] M. A. L. Bell, X. Guo, H. J. Kang, and E. Boctor, "Improved contrast in laser-diode-based photoacoustic images with short-lag spatial coherence beamforming," in *2014 IEEE International Ultrasonics Symposium*, 2014, pp. 37-40.

[3] E. A. Gonzalez and M. A. L. Bell, "GPU implementation of photoacoustic short-lag spatial coherence imaging for improved image-guided interventions," *Journal of Biomedical Optics,* vol. 25, p. 077002, 2020.

[4] R. A. Mukaddim and T. Varghese, "Spatiotemporal Coherence Weighting for *In Vivo* Cardiac Photoacoustic Image Beamformation," *IEEE transactions on ultrasonics, ferroelectrics, and frequency control* 2020.

[5] B. Pourebrahimi, S. Yoon, D. Dopsa, and M. C. Kolios, "Improving the quality of photoacoustic images using the short-lag spatial coherence imaging technique," in *Photons Plus Ultrasound: Imaging and Sensing 2013*, 2013, p. 85813Y.

[6] Y.-H. Wang and P.-C. Li, "SNR-dependent coherence-based adaptive imaging for high-frame-rate ultrasonic and photoacoustic imaging," *IEEE transactions on ultrasonics, ferroelectrics, and frequency control,* vol. 61, pp. 1419-1432, 2014.

[7] T. Kirchner, F. Sattler, J. Gröhl, and L. Maier-Hein, "Signed real-time delay multiply and sum beamforming for multispectral photoacoustic imaging," *Journal of Imaging,* vol. 4, p. 121, 2018.

[8] M. Mozaffarzadeh, A. Hariri, C. Moore, and J. V. Jokerst, "The double-stage delay-multiply-and-sum image reconstruction method improves imaging quality in a led-based photoacoustic array scanner," *Photoacoustics,* vol. 12, pp. 22-29, 2018.

[9] J. Park, S. Jeon, J. Meng, L. Song, J. S. Lee, and C. Kim, "Delay-multiply-and-sum-based synthetic aperture focusing in photoacoustic microscopy," *Journal of biomedical optics,* vol. 21, p. 036010, 2016.

[10] M. W. Kim, G.-S. Jeng, I. Pelivanov, and M. O'Donnell, "Deep-learning Image Reconstruction for Real-time Photoacoustic System," *IEEE Transactions on Medical Imaging,* 2020.

[11] D. Allman, A. Reiter, and M. A. L. Bell, "Photoacoustic source detection and reflection artifact removal enabled by deep learning," *IEEE transactions on medical imaging,* vol. 37, pp. 1464-1477, 2018.

[12] K. Johnstonbaugh, S. Agrawal, D. A. Durairaj, C. Fadden, A. Dangi, S. P. K. Karri*, et al.*, "A deep learning approach to photoacoustic wavefront localization in deep-tissue medium," *IEEE Transactions on Ultrasonics, Ferroelectrics, and Frequency Control,* 2020.

[13] H. Lan, D. Jiang, C. Yang, F. Gao, and F. Gao, "Y-Net: Hybrid deep learning image reconstruction for photoacoustic tomography in vivo," *Photoacoustics,* vol. 20, p. 100197, 2020.

[14] M. Mozaffarzadeh, A. Mahloojifar, M. Orooji, K. Kratkiewicz, S. Adabi, and M. Nasiriavanaki, "Linear-array photoacoustic imaging using minimum variance-based delay multiply and sum adaptive beamforming algorithm," *Journal of biomedical optics,* vol. 23, p. 026002, 2018.

[15] M. Mozaffarzadeh, A. Mahloojifar, M. Nasiriavanaki, and M. Orooji, "Eigenspace-based minimum variance adaptive beamformer combined with delay multiply and sum: experimental study," in *Photonics in Dermatology and Plastic Surgery 2018*, 2018, p. 1046717.

[16] R. Paridar, M. Mozaffarzadeh, M. Mehrmohammadi, and M. Orooji, "Photoacoustic image formation based on sparse regularization of minimum variance beamformer," *Biomedical Optics Express,* vol. 9, pp. 2544-2561, 2018.

[17] S. Shamekhi, V. Periyasamy, M. Pramanik, M. Mehrmohammadi, and B. M. Asl, "Eigenspace-based minimum variance beamformer combined with sign coherence factor: Application to linear-array photoacoustic imaging," *Ultrasonics,* p. 106174, 2020.

[18] R. A. Mukaddim, A. M. Weichmann, and T. Varghese, "Photoacoustic Delay-and-Sum Beamforming with Spatiotemporal Coherence Factor," *2020 IEEE International Ultrasonics Symposium (IUS), IEEE, 2020.,* 2020.

[19] R. A. Mukaddim, R. Ahmed, and T. Varghese, "Sub-aperture Processing Based Adaptive Beamforming for Photoacoustic Imaging," *IEEE transactions on ultrasonics, ferroelectrics, and frequency control* 2021.

[20] J.-F. Synnevag, A. Austeng, and S. Holm, "Benefits of minimum-variance beamforming in medical ultrasound imaging," *IEEE transactions on ultrasonics, ferroelectrics, and frequency control,* vol. 56, pp. 1868-1879, 2009.

[21] C. H. Seo and J. T. Yen, "Sidelobe suppression in ultrasound imaging using dual apodization with cross-correlation," *IEEE transactions on ultrasonics, ferroelectrics, and frequency control,* vol. 55, pp. 2198-2210, 2008.

[22] J. T. Yen and C. H. Seo, "Sidelobe suppression in ultrasound imaging using dual apodization with cross-correlation," ed: Google Patents, 2012.

[23] B. E. Treeby and B. T. Cox, "k-Wave: MATLAB toolbox for the simulation and reconstruction of photoacoustic wave fields," *Journal of biomedical optics,* vol. 15, p. 021314, 2010.

[24] L. R. Dixon, "The complete blood count: physiologic basis and clinical usage," *The Journal of perinatal & neonatal nursing,* vol. 11, pp. 1-18, 1997.

[25] J. Staal, M. D. Abràmoff, M. Niemeijer, M. A. Viergever, and B. Van Ginneken, "Ridge-based vessel segmentation in color images of the retina," *IEEE transactions on medical imaging,* vol. 23, pp. 501-509, 2004.

[26] D. Marti, R. N. Aasbjerg, P. E. Andersen, and A. K. Hansen, "MCmatlab: an open-source, user-friendly, MATLAB-integrated three-dimensional Monte Carlo light transport solver with heat diffusion and tissue damage," *Journal of biomedical optics,* vol. 23, p. 121622, 2018.

[27] K. M. Kempski, M. T. Graham, M. R. Gubbi, T. Palmer, and M. A. L. Bell, "Application of the generalized contrast-to-noise ratio to assess photoacoustic image quality," *Biomedical Optics Express,* vol. 11, pp. 3684-3698, 2020.

[28] A. Rodriguez-Molares, O. M. H. Rindal, J. D'hooge, S.-E. Måsøy, A. Austeng, M. A. L. Bell*, et al.*, "The generalized contrast-to-noise ratio: a formal definition for lesion detectability," *IEEE Transactions on Ultrasonics, Ferroelectrics, and Frequency Control,* vol. 67, pp. 745-759, 2019.